

SIMULATION ANALYSIS OF DYNAMIC PROPERTIES OF MOC-SLP AFTER FREEZE-THAW CYCLES

Chai, S. Q.*; Shang, H.*; Liu, X. Q.*#; Wang, S. R.** & Gong, J.**

* China Communications First Highway Group Co., Ltd. Seventh Engineering Company, Xinmi 452370, China

** School of Civil Engineering, Henan Polytechnic University, Jiaozuo 454003, China

E-Mail: CFHEC_7GS@foxmail.com (# Corresponding author)

Abstract

To reveal the dynamic mechanical properties of magnesium oxychloride cement-stone powder (MOC-SLP) after freeze-thaw cycles under high strain rates, a computational model of the split Hopkinson pressure bar was constructed using ANSYS/LS-DYNA. The dynamic impact process under different impact velocities was simulated, combined with the variable of 0-20 freeze-thaw cycles. The dynamic stress-strain response, energy absorption characteristics, and failure morphology evolution were analysed. The entire dynamic damage process of specimens was tracked also. Results show that MOC-SLP exhibits significant strain rate hardening effects. MOC-SLP still maintains strain rate sensitivity after freeze-thaw cycles, but the hardening amplitude decreases, reflecting the dynamic load-bearing potential of damaged specimens. As the number of freeze-thaw cycles increases, the failure mode of specimens transforms from axial tensile failure to shear-tensile composite failure, with aggravated brittle failure characteristics and more fragmented failure morphology. This study provides the theoretical support for their application in impact and explosion protection environments.

(Received in September 2025, accepted in January 2026. This paper was with the authors 2 weeks for 1 revision.)

Key Words: Magnesium Oxychloride Cement, Stone Powder, Strain Rate Effect, Numerical Simulation, Failure Mode

1. INTRODUCTION

In the field of building material performance research under freeze-thaw environments, traditional cement-based materials suffer from structural damage due to water expansion and contraction induced by freeze-thaw cycles, limiting their application in low-temperature environments. However, the long-term durability research of magnesium oxychloride cement (MOC) as a green and eco-friendly alternative material remains insufficient. The influence mechanism of industrial waste-stone powder (SLP) content on the freeze-thaw performance of MOC is unclear, particularly under cyclic loading conditions after freeze-thaw cycles. The evolution laws of dynamic mechanical properties, energy absorption characteristics, and failure mode evolution mechanisms of MOC-SLP composites under high strain rates after freeze-thaw cycles have not been fully elucidated, lacking systematic theoretical models and quantitative analysis methods [1-3].

Current research bottlenecks primarily include the following: While the freeze-thaw damage mechanism of traditional cement-based materials is well-established, the correlation between microstructural evolution and macroscopic performance degradation of MOC under long-term freeze-thaw environments remains underexplored. The impact of SLP content on the freeze-thaw performance of MOC has been the subject of controversy, with no unified content standards or performance evaluation metrics. A gap exists between numerical simulation and experimental validation of the stress-strain response, energy transfer paths, and full-process damage evolution of MOC-SLP composites under dynamic impact after freeze-thaw cycles. The influence mechanism of freeze-thaw damage on the failure modes of MOC-SLP composites has not been fully revealed, affecting the reliability of their application in harsh environments such as impact and explosion protection [4, 5].

This study focuses on the evolution laws of the dynamic mechanical behaviour of MOC-SLP composites under the coupled effects of freeze-thaw impact. It validates the applicability of the split Hopkinson pressure bar (SHPB) numerical simulation method in complex environments and clarifies the suppression mechanism of SLP content on freeze-thaw damage. This research provides theoretical foundations and technical support for material optimization design, structural stability assessment, and industrial waste recycling in cold regions for impact/explosion protection scenarios, contributing to the enhancement of building material durability and safety.

2. STATE OF THE ART

Freeze-thaw cycling represents a core environmental challenge for building materials in cold regions, as it induces internal stress concentration in materials through the repeated expansion and contraction of moisture, leading to crack initiation, propagation, and strength degradation, which severely compromises structural durability. Focusing on this issue, some scholars have conducted relevant research. For instance, Gong et al. [6] investigated the coupled mechanical-microstructural damage behaviour of phosphoric acid-modified MOC under dry-wet-freeze-thaw cycling. Misra and Mathur [7] evaluated the mechanical properties and durability of MOC concrete under extreme environmental conditions. Hamada et al. [8] evaluated the research progress on improving the water resistance of MOC. Wang et al. [9] analysed the dynamic properties of MOC-titanium gypsum composites after freeze-thaw cycles. While Yang et al. [10] investigated the deterioration mechanism of the interface transition zone in concrete pavement under the combined effects of fatigue loading and freeze-thaw cycles in cold climates.

In the research on the coupling mechanism of cyclic loading and freeze-thaw conditions, Wu et al. [11] investigated the damage mechanism of sawdust-MOC composites under uniaxial compressive load using AE and DIC techniques. Cao et al. [12] studied the influence of highland barley straw ash prepared under certain conditions on the durability of MOC mortar under freeze-thaw damage. Ahmad et al. [13] investigated the mechanical behaviour of MOC-based composites reinforced with hybrid fibres. Kia et al. [14] evaluated the freeze-thaw durability of conventional and innovative permeable pavement materials, comparing their performance under cyclic freezing and thawing conditions to assess long-term structural integrity. Hanjari et al. [15] conducted an experimental investigation into the material and bond properties of frost-damaged concrete, analysing how freeze-thaw cycles affect mechanical behaviour and interfacial adhesion. But these studies lacked complex environmental analysis and robust long-term modelling.

The core issues in current research are prominently manifested in three aspects: First, there is a lack of quantitative analysis on the influence paths of stone powder content on the freeze-thaw performance of MOC-SLP materials (such as the evolution of crystal structure in the interfacial transition zone and changes in porosity). The laws of internal stress distribution, micro-crack propagation, and damage evolution in materials under the coupling conditions of freeze-thaw and cyclic loading have not been revealed [16]. Second, there is a lack of systematic experimental data on the interaction between different stone powder contents and freeze-thaw cycles on the mechanical properties of materials, making it impossible to establish an accurate performance prediction model and limiting the reliability assessment for engineering applications [17, 18]. Third, the existing research has not clearly defined the optimal range of stone powder content for MOC-SLP materials in engineering projects in cold regions. There is a lack of performance improvement solutions based on actual working conditions, such as multiple freeze-thaw cycles and dynamic loading, resulting in uncertainties in the durability and assessment of materials under extreme conditions [19, 20].

This study focuses on MOC-SLP composite materials, addressing the lack of systematic stone powder content gradients by setting five stone powder content levels (0–40%) and three freeze-thaw cycle counts to quantitatively analyse the synergistic effect of stone powder content and freeze-thaw environments [21, 22]. Using LS-DYNA to simulate dynamic impacts at strain rates ranging from $10^{-4}/s$ to $10^{-2}/s$, combined with plastic strain energy tracking technology, a correlation between energy dissipation and damage evolution is established, overcoming the limitation of focusing solely on strength indicators. By integrating SEM/CT imaging with fractal theory, a full dynamic evolution model for microcrack initiation, propagation, and collapse is constructed, correcting the applicability limitations of previous studies in cold regions. Combined with gradient design of steel fibre parameters, the fibre regulation mechanism is clarified. Finally, through high-temperature and corrosion coupled experimental validation of fatigue criteria, engineering reliability is ensured. This research achieves full-scale dynamic tracking from micro to macro scales, providing a scientific basis for the design of infrastructure in cold regions.

3. METHODOLOGY

3.1 Computational model

The influence mechanism of dynamic loading on the stress wave loading-unloading characteristics of intact MOC-SLP specimens was elucidated by using LS-DYNA software to perform SHPB impact simulation calculations on the specimens [23]. The stress evolution laws and fragmentation behaviours of specimens under different impact velocities were analysed.

A 1:1 scale simulation of the SHPB test device was adopted to faithfully replicate the SHPB apparatus used in laboratory experiments. A three-dimensional (3D) model was constructed using the ANSYS/LS-DYNA. The computational model consists of three parts: an incident bar, a specimen, and a transmission bar, with diameters of 50 mm and lengths of 2000, 25, and 1400 mm, respectively. The model comprises a total of 183,000 elements for both the specimen and the bars. Fig. 1 illustrates the mesh division at the interface between the MOC-SLP specimen and the elastic bars. Fig. 2 shows the mesh division of the MOC-SLP specimen.

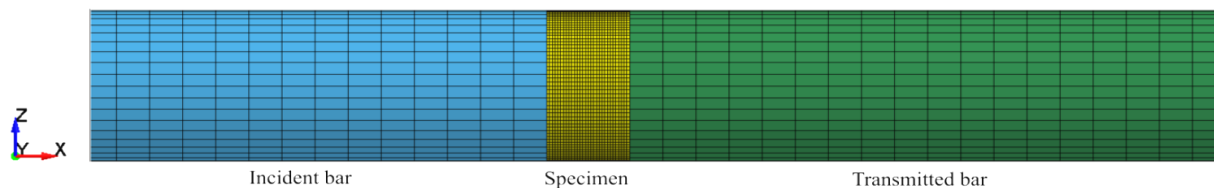


Figure 1: The computational model.

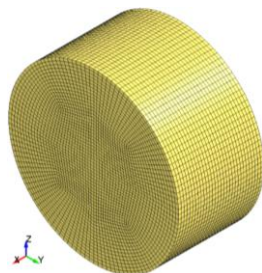


Figure 2: Mesh division of the MOC-SLP specimen.

The projectile was not modelled directly in this numerical simulation test. Instead, a load curve was applied at the end of the incident bar to simulate the impact process. The applied

load curve was derived by simulating the near-rectangular stress pulse that is generated when a cylindrical projectile strikes the incident bar. Different strain rate loadings were achieved by varying the amplitude of the load curve. Fig. 3 shows the simulated applied load curves under different strain rates. The impact voltage increases, and the amplitude of the applied load curve continuously rises.

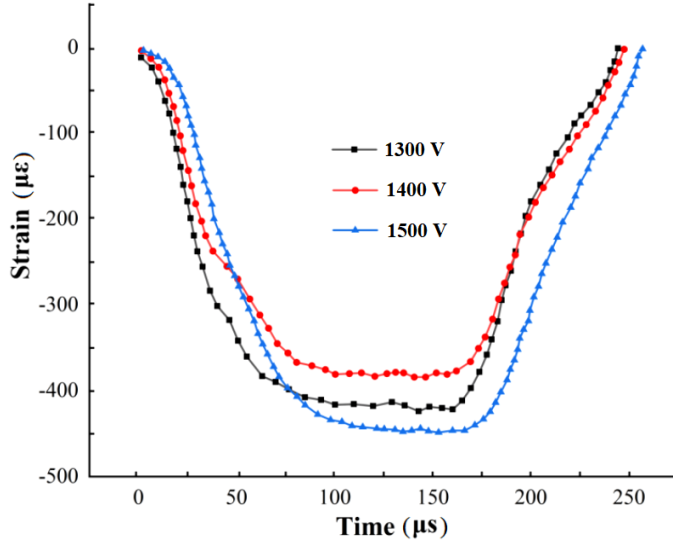


Figure 3: Simulated load application curves at different strain rates.

3.2 Selection of constitutive model and parameters

The Holmquist-Johnson-Cook (HJC) constitutive model [24, 25] is a phenomenological model that is widely applied to describe the dynamic mechanical behaviour of brittle materials (concrete, rock, etc.) under high strain rates, high pressures, and damage conditions. This model integrates the pressure-volume relationship, deviatoric stress response, and damage evolution, thus being able to effectively simulate the mechanical response of materials under extreme loads such as impact, explosion, or penetration (Fig. 4).

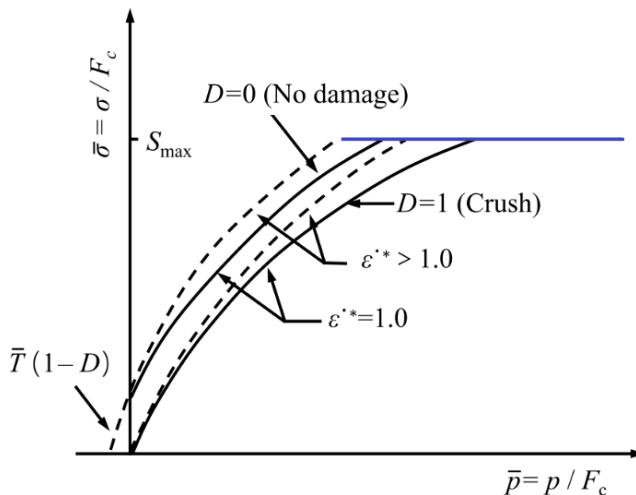


Figure 4: Yield surface equation.

The yield surface equation of the HJC model is defined based on normalized equivalent stress, with the corresponding expression given as:

$$\sigma^* = [A(1-D) + BP^{*N}] \left[1 + C \ln \varepsilon^* \right] \leq S_{\max} \quad (1)$$

where, σ^* represents the ratio of the equivalent stress to the uniaxial compressive strength f_c . σ represents the ratio of hydrostatic pressure P to the uniaxial compressive strength f_c . ε^* represents the ratio of the true strain rate ε to the reference strain rate ε^0 . A and B represent the normalized cohesion strength coefficient and the normalized pressure coefficient, respectively. N and C represent the strain hardening index and the strain rate coefficient, respectively. D represents the damage coefficient determined by the damage function, and its value range is from 0 to 1. S_{\max} represents the maximum normalized strength.

The HJC model describes the damage caused by the reduction in bonding strength due to the compaction of internal voids in the material through the accumulation of equivalent plastic strain and plastic volume strain, and the corresponding expression is as follows:

$$D = \sum \frac{\Delta\varepsilon_p + \Delta\mu_p}{\varepsilon_p^f + \mu_p^f} \quad (2)$$

$$\varepsilon_p^f + \mu_p^f = D_1(P^* + T^*)^{D_2} \geq EFMIN \quad (3)$$

where, $\Delta\varepsilon_p$ and ε_p^f represents the equivalent plastic strain and the increment of equivalent plastic strain of the material at normal pressure, respectively. μ_p^f and $\Delta\mu_p$ represents the plastic volumetric strain and the increment of plastic volumetric strain of the material at normal pressure, respectively. $EFMIN$ represents the minimum plastic strain when the material fails. D_1 and D_2 represent the control of the degree of material damage parameters. T^* represents the ratio of the maximum tensile strength to uniaxial compressive strength f_c . When $P^* = -T^*$, the material is no longer subjected to any plastic strain.

The hydrostatic pressure-volume strain curve of the material in the HJC model is composed of piecewise state equations, as shown in Fig. 5.

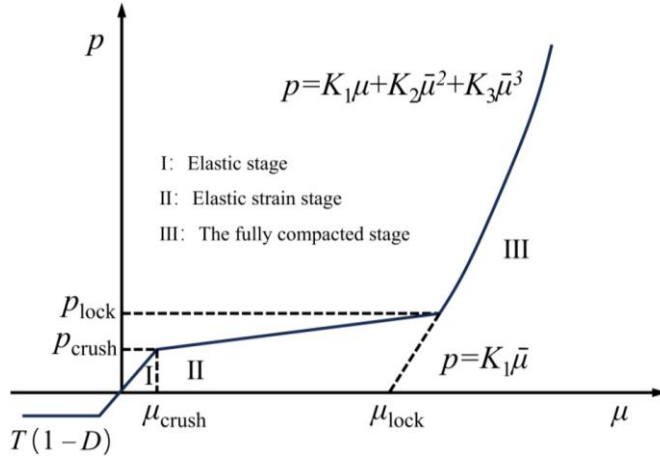


Figure 5: Hydrostatic pressure-volume strain equation.

The first stage is the linear elastic stage ($-T(1-D) \leq P \leq P_{crush}$), where the hydrostatic pressure and volumetric strain show a linear relationship. That is, both the loading section and the unloading section are reversible elastic states, and the expression is:

$$P = k_e \mu \quad (4)$$

$$k_e = \frac{P_{crush}}{\mu_{crush}} \quad (5)$$

where, k_e and μ represent the elastic bulk modulus and volumetric strain, respectively. k_e is the ratio of the hydrostatic pressure P_{crush} to the volumetric strain μ_{crush} when the material reaches the elastic limit in the uniaxial compression test.

The second stage is the plastic strain stage ($P_{\text{crush}} < P \leq P_{\text{lock}}$), where the internal voids of the material gradually compact, and plastic volumetric strain and destructive cracks begin to appear. The expressions are:

$$P = (\mu - \mu_{\text{crush}})k_p + P_{\text{crush}} \quad (6)$$

$$P = P_0 - [(1-F)K_p + FK_1](\mu_0 - \mu) \quad (7)$$

where, $k_p = (P_{\text{lock}} - P_{\text{crush}})/(\mu_{\text{lock}} - \mu_{\text{crush}})$ represents the plastic bulk modulus. P_{lock} and μ_{lock} represent the compacted hydrostatic pressure and volumetric strain, respectively. P_0 and μ_0 represent the hydrostatic pressure and volumetric strain before unloading, respectively. F represents the unloading ratio coefficient $K_p = (\mu_0 - \mu_{\text{lock}})/(\mu_{\text{lock}} - \mu_{\text{crush}})$.

The third stage is the complete compaction section ($P > P_{\text{lock}}$), where all the voids inside the material are compacted, resulting in material failure. The expression is:

$$P = K_1 \bar{\mu} \quad (8)$$

where, K_1 represents the pressure constant of the fully compacted material, and $\bar{\mu}$ represents the corrected volumetric strain $\bar{\mu} = (\mu - \mu_{\text{lock}})/(1 + \mu_{\text{lock}})$.

The dynamic constitutive model of concrete HJC has a total of 19 computational parameters. Along with the other two software parameters, EPSO and FS, the HJC parameter model in the numerical simulation has a total of 21 items. The calibration steps for the key parameters of the HJC model in this study are as follows.

The basic parameters of the material are ρ (kg/m^3), f_c (Pa), T (Pa), and G (Pa). The elastic modulus T and shear modulus G are determined by the following formula:

$$T = 0.62 \cdot f_c^{0.5} \quad (9)$$

$$G = E / (1 + 2\nu) \quad (10)$$

where, T and G represent the elastic modulus and shear modulus, respectively. ν represents the Poisson's ratio.

The material damage parameters are D_1 , D_2 , and D . The damage function D is automatically calculated by the program. For ordinary concrete, the value is 0.01, and D_2 is taken as the initial value of 1.0. D_1 is determined by the following formula:

$$D_1 = \frac{2(1-\nu)\varepsilon_p^f}{(1/6 + T^*)^{D_2}} \quad (11)$$

where ε_p^f represents the equivalent plastic strain at which concrete materials fail under normal pressure, and T^* represents the ratio of the maximum tensile strength T to the uniaxial compressive strength f_c .

The material pressure parameters are K_1 , K_2 , K_3 , P_{crush} , μ_{crush} , P_{lock} , and μ_{lock} . Among them, K_1 , K_2 , and K_3 are parameters of the stress-strain curve after the concrete is compacted. The strain rate range of the material SHPB experiment causes the material not to enter the compaction section under load. Therefore, the simulation calculation range is only in the second stage of the p - μ curve, while parameters K_1 , K_2 , and K_3 control the complete compaction stage (the third stage) of the p - μ curve. Thus, the influence of parameters K_1 , K_2 , and K_3 on the stress-strain curve is extremely small. Linear interpolation is adopted to obtain the value P_{lock} of LP-LAMOC [26], and the calculation formula is:

$$P_{\text{lock}} = 0.8 + \frac{f_c - 48}{460} (f_c < 140) \quad (12)$$

$$P_{\text{lock}} = 1 + \frac{f_c - 140}{460} (f_c > 140)$$

The calculation formulas for the other three parameters μ_{crush} , P_{crush} and μ_{lock} are as follows:

$$P_{\text{crush}} = \frac{1}{3}f_c$$

$$\mu_{\text{crush}} = \frac{3P_{\text{crush}}(1-2\nu)}{E} \quad (13)$$

$$\mu_{\text{lock}} = \frac{\rho_c'}{\rho_0 - \rho_f V_f + \rho_c' V_f} - 1$$

where, ρ_0 represents the apparent density of fibre-reinforced concrete, ρ_f indicates the density of steel fibres, ρ_c' indicates the compaction density of plain concrete, and V_f indicates the volume content of steel fibres.

The strength parameters of the material are A , B , C , N , and S_{max} . According to existing research, the strain rate coefficient C has a relatively small influence on the yield surface equation. For MOC-SLP, the value of C is 0.007. B and N need to be obtained through the given A by fitting the stress-pressure normalized curve. The parameters of the HJC model are shown in Table I.

Table I: Parameters of the HJC model.

ρ (kg/m ³)	G (GPa)	A	B	N	C	f_c (MPa)
1588	11.30	0.42	2.11	0.78	0.01	38.0
f_t (MPa)	$EFMIN$	S_{max}	P_{crush} (MPa)	μ_{crush}	P_{lock} (MPa)	μ_{lock}
3.60	0.01	4.00	12.0	0.001	1200	0.10
D_1	D_2	K_1 (GPa)	K_2 (GPa)	K_3 (GPa)	f_s	$MXEPS$
0.03	1.00	20.0	-100	500	0.003	0.10

3.3 Simulation analysis scheme

This study focuses on MOC-SLP composites, establishing five groups of SLP content (0 %, 10 %, 20 %, 30 %, 40 %) and three groups of freeze-thaw cycle numbers (0, 10, and 20). With the use of ANSYS/LS-DYNA, an SHPB numerical model was constructed to simulate dynamic impact processes under three different impact velocities (strain rates). The analysis includes dynamic stress-strain response, energy absorption characteristics, and failure morphology evolution, combined with freeze-thaw cycle variables. The entire dynamic damage process from microcrack initiation to propagation to crushing were tracked. Mechanical behaviour differences between unfrozen and freeze-thawed specimens under different strain rates were compared. This protocol systematically investigates the coupled effects of SLP content, freeze-thaw cycles, and strain rates on the dynamic performance of MOC-SLP composites.

4. RESULTS ANALYSIS AND DISCUSSION

4.1 Variation characteristics of dynamic stress wave

The diameter of the Hopkinson rod will increase with the increase in the specimen size to ensure the macroscopic uniformity of the MOC-SLP specimens. Therefore, evaluating the discrete effect of stress waves in SHPB testing is particularly important. Fig. 6 shows the distribution of the axial stress of Hopkinson rods at different times.

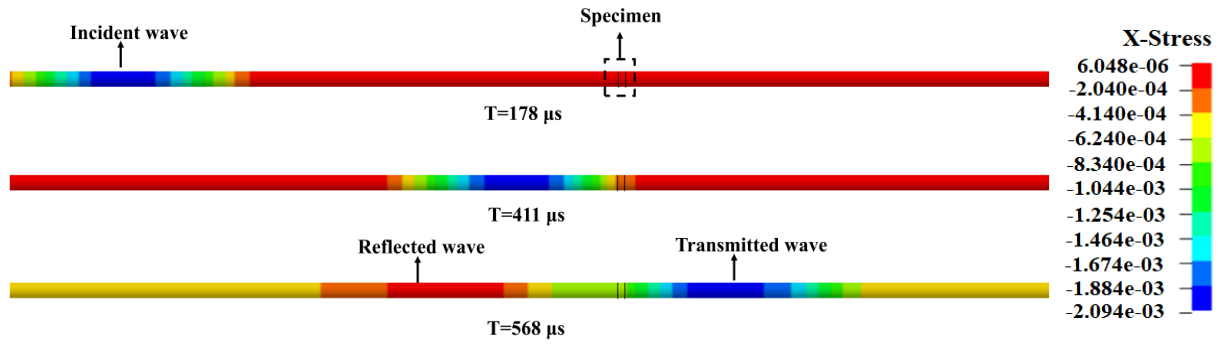


Figure 6: The propagation process of stress waves in the test at different times.

As seen from Fig. 6, when the stress wave is transmitted into the incident rod, the axial stress wave propagates uniformly along the incident rod in the form of a compression wave at $T = 178 \mu\text{s}$. The stress wave propagates along the incident rod to the surface of the sample at $T = 411 \mu\text{s}$, and it completes reflection and transmission on the surface of the sample at $T = 568 \mu\text{s}$, forming a reflected wave and a transmitted wave. Throughout the entire process, the radial stress remains at a relatively small value. The size of the zone element for constructing the compression bar also affects the dispersion of the stress wave.

Fig. 7 shows the axial stress waves in the Hopkinson rod. The axial stress waves in the Hopkinson rod are detected by extracting the specified elements on the surface of the incident rod and the transmitted rod, and the transmitted stress waves are captured by capturing the strain.

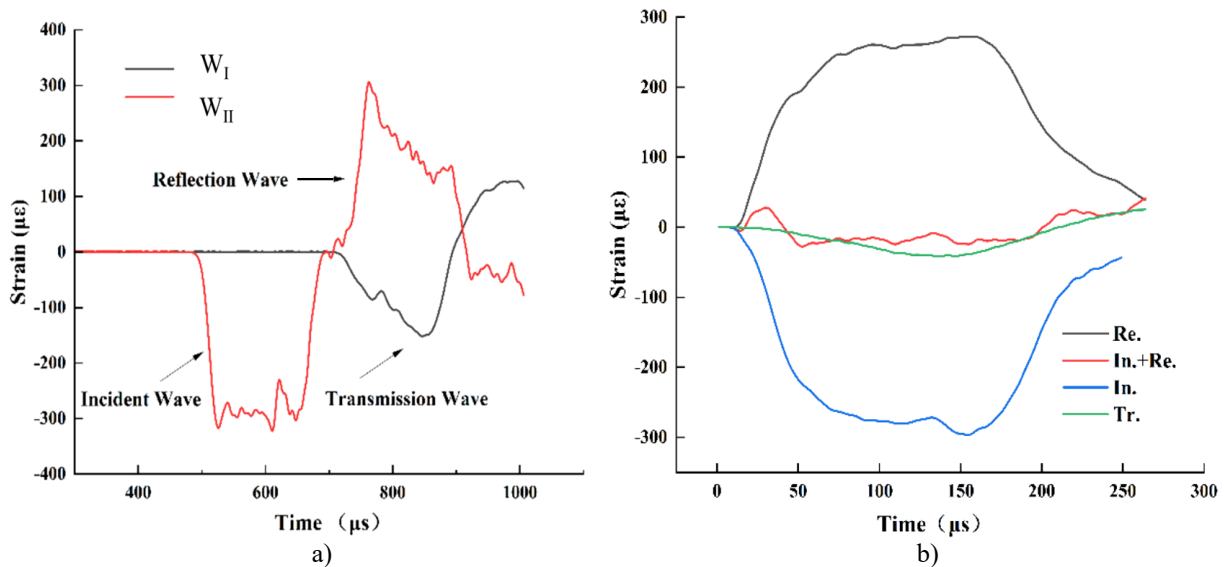


Figure 7: Stress wave propagation in the Hopkinson bar; a) Stress wave time-history curves, b) Stress wave equilibrium diagram.

4.2 Variation characteristics of dynamic stress-strain curves

Fig. 8 shows the dynamic stress-strain curve of the specimen under simulated impact loading. During the simulated impact process, the dynamic peak stress of the specimen exceeded the yield strength of the material. The specimen underwent irreversible macroscopic damage, resulting in a continuous increase in deformation, while the stress continued to decrease. The general shape is an open-type stress-strain curve, and no obvious stress rebound phenomenon occurs in the post-peak stage of this type of curve.

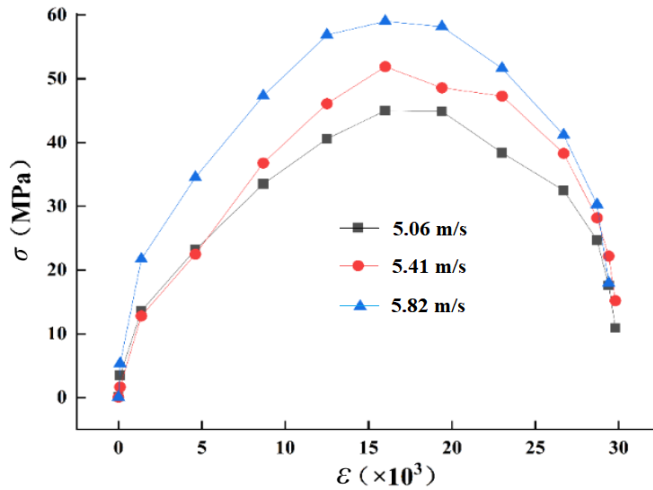


Figure 8: Dynamic stress-strain curves of the specimens at different strain rates.

At the initial stage of the simulation loading, the units where the sample was damaged in the numerical simulation were directly deleted. In the actual test, this part still has a certain bearing capacity. The simulation assumes that the sample is a homogeneous isotropic material, but in reality, the sample itself has a certain degree of non-uniformity. Thus, the dynamic stress-strain curve of the sample obtained from the simulation will have certain differences from the test results.

4.3 Dynamic failure process analysis of specimens

The dynamic failure process of the specimen under a strain rate of 78.24 s^{-1} is shown in Fig. 9.

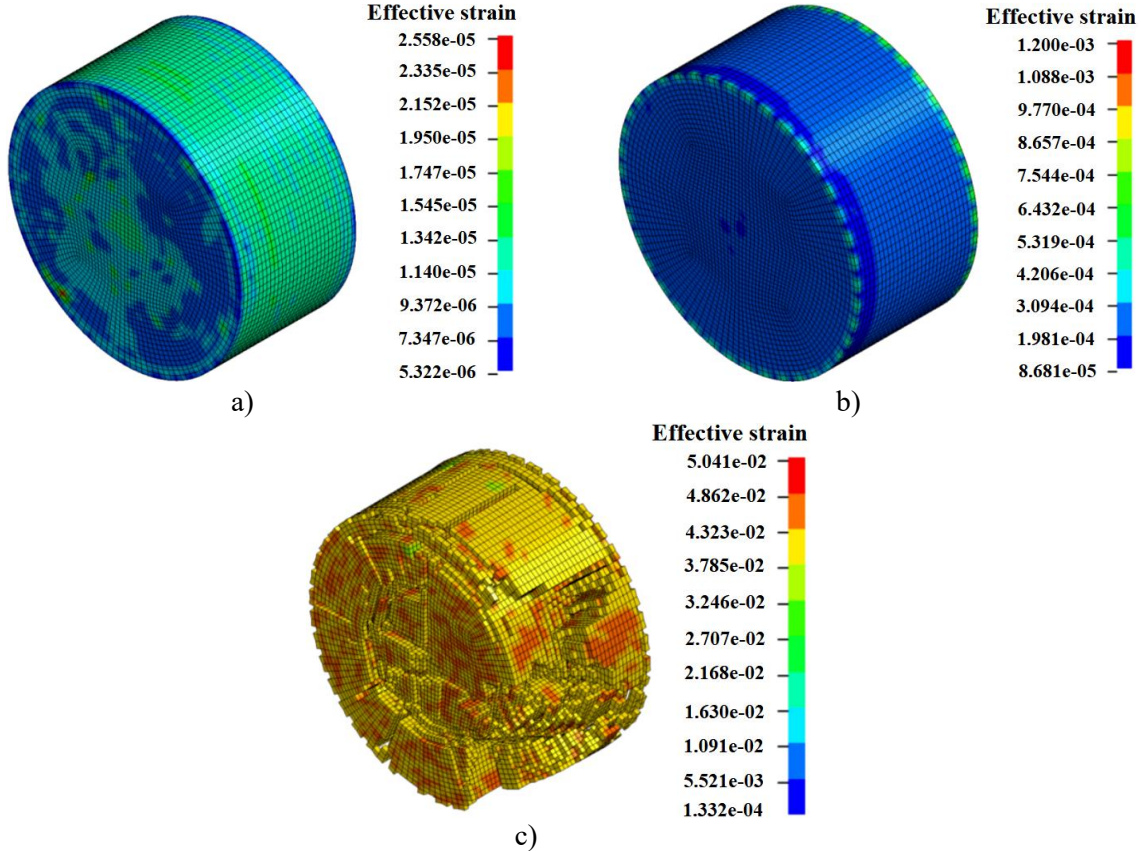


Figure 9: The dynamic failure process of the specimen under a strain rate of 78.24 s^{-1} ; a) $411 \mu\text{s}$; b) $568 \mu\text{s}$; c) $856 \mu\text{s}$.

As depicted in Fig. 9 a, the stress wave propagates to the specimen within 411 μs . Subsequently, the stress wave reflects back and forth within the specimen. Stress is concentrated significantly at the specimen's end boundaries as a result of boundary effects. The incident stress wave continuously penetrates the specimen interior, accumulating stress over time.

At $T = 568 \mu\text{s}$, when the compressive stress wave reaches the free surfaces of the MOC-SLP specimen, it reflects back as tensile waves. The tensile strength of MOC-SLP is significantly lower than its compressive strength; thus, the combined effects of boundary conditions and tensile waves cause the elements at the specimen's peripheral sections to reach their load-bearing limit first, leading to sequential failure and spalling of these elements (Fig. 9 b). This condition results in tensile strain failure at this stage.

As the stress wave continues to act, at $T = 856 \mu\text{s}$, axial tensile cracks develop around the specimen's periphery and propagate radially toward the centre. The failure mode transitions from tensile strain failure to axial splitting failure (Fig. 9 c).

5. CONCLUSIONS

Taking the freeze-thaw cycled MOC-SLP composites as the research object, this study established an SHPB numerical model using ANSYS/LS-DYNA to simulate dynamic impact processes under varying impact velocities and freeze-thaw cycle counts. The evolution of dynamic mechanical properties was analysed, and mechanical behaviour differences between freeze-thawed and intact specimens were compared. The main conclusions are obtained as follows:

(1) The freeze-thawed MOC-SLP material retains strain rate sensitivity. Under different impact velocities, its dynamic strength and energy absorption efficiency still increase with rising strain rates, demonstrating a typical strain rate hardening effect. However, the magnitude of enhancement is reduced compared with that of unfrozen specimens, reflecting residual dynamic load-bearing potential despite internal structural damage.

(2) With increasing freeze-thaw cycles, the failure mode of specimens transitions from typical axial tensile failure to mixed shear-tensile failure, indicating that the stress distribution patterns within the material are evolving. Numerical simulations clearly reveal the impact of freeze-thaw damage on failure mechanisms.

(3) Simulation results show that freeze-thawed specimens exhibit enhanced brittle failure characteristics under dynamic impact, with more fragmented failure morphologies. The simulations visually confirm that initial freeze-thaw-induced damage acts as stress concentration points, accelerating and intensifying final material instability and fragmentation.

The SHPB numerical model developed in this study effectively reproduces the dynamic response, energy transmission, and damage evolution processes of freeze-thawed MOC-SLP specimens. It serves as an economical and reliable analytical tool for investigating the impact resistance of such materials in harsh environments. Future work will incorporate temperature and humidity variables to enhance the model's practical applicability, explore its application potential in broader extreme environments, and provide theoretical foundations for improving the durability and safety of construction materials.

ACKNOWLEDGMENT

This work was financially supported by the National Scholarship Fund of China [2023]-21, the Key Project of Natural Science Foundation of Henan Province, China (232300421134), the First-Class Discipline Implementation of Safety Science and Engineering (AQ20230103), and the Zhongyuan Science and Technology Innovation Leading Talent Program (244200510005), China.

REFERENCES

- [1] Li, H.; Guo, H.-L.; Zhang, Y. (2022). Deterioration of concrete under the coupling action of freeze-thaw cycles and salt solution erosion, *Reviews on Advanced Materials Science*, Vol. 61, No. 1, 322-333, doi:[10.1515/rams-2022-0025](https://doi.org/10.1515/rams-2022-0025)
- [2] Poklemba, R.; Duplakova, D.; Zajac, J.; Duplak, J.; Simkulet, V.; Goldyniak, D. (2020). Design and investigation of machine tool bed based on polymer concrete mixture, *International Journal of Simulation Modelling*, Vol. 19, No. 2, 291-302, doi:[10.2507/IJSIMM19-2-518](https://doi.org/10.2507/IJSIMM19-2-518)
- [3] Kolarova, M.; Klouzkova, A.; Jankovsky, O.; Lauermannova, A. M.; Zaleska, M.; Pivak, A.; Pavlikova, M.; Pavlik, Z. (2025). The effect of application of waste glass cullet as a filler in a cleaner production of magnesium oxychloride cement composites, *Construction and Building Materials*, Vol. 482, Paper 141649, 14 pages, doi:[10.1016/j.conbuildmat.2025.141649](https://doi.org/10.1016/j.conbuildmat.2025.141649)
- [4] Esmaeili, M.; Behnajad, S.; Esfahani, M. H. (2023). Laboratory investigation on preplaced ballast aggregate concrete deterioration over freezing-thawing cycles, *International Journal of Concrete Structures and Materials*, Vol. 17, No. 1, Paper 45, 24 pages, doi:[10.1186/s40069-023-00606-3](https://doi.org/10.1186/s40069-023-00606-3)
- [5] Kim, S.; Lee, J.; Hong, Y.; Choi, W.; Kim, J. (2025). Assessing the durability of biochar concrete: performance under freeze-thaw cycles, *Advances in Concrete Construction*, Vol. 19, No. 6, 381-391, doi:[10.12989/acc.2025.19.6.381](https://doi.org/10.12989/acc.2025.19.6.381)
- [6] Gong, J.; Zhang, J.-X.; Wang, S.-R.; Ma, A.-C.; An, Z.-Z. (2026). Coupled mechanical-microstructural damage behavior of phosphoric acid-modified MOC under dry-wet-freeze-thaw cycling, *Case Studies in Construction Materials*, Vol. 24, Paper e05693, 25 pages, doi:[10.1016/j.cscm.2025.e05693](https://doi.org/10.1016/j.cscm.2025.e05693)
- [7] Misra, A. K.; Mathur, R. (2007). Magnesium oxychloride cement concrete, *Bulletin of Materials Science*, Vol. 30, No. 3, 239-246, doi:[10.1007/s12034-007-0043-4](https://doi.org/10.1007/s12034-007-0043-4)
- [8] Hamada, H. M.; Al-Attar, A.; Askar, M. K.; Beddu, S.; Majdi, A. (2025). Research progress on improving the water resistance of magnesium oxychloride cement (MOC), *International Journal of Concrete Structures and Materials*, Vol. 19, No. 1, Paper 76, 21 pages, doi:[10.1186/s40069-025-00808-x](https://doi.org/10.1186/s40069-025-00808-x)
- [9] Wang, S.-R.; Song, Z.-H.; Gong, J.; Kim, M.; Rabe, M. (2025). Dynamic properties of magnesium oxychloride-titanium gypsum mineral material after freeze-thaw cycles, *Acta Montanistica Slovaca*, Vol. 30, No. 1, 142-153, doi:[10.46544/AMS.v30i1.11](https://doi.org/10.46544/AMS.v30i1.11)
- [10] Yang, X.-L.; Shen, A.-Q.; Guo, Y.-C.; Zhou, S.-B.; He, T.-Q. (2018). Deterioration mechanism of interface transition zone of concrete pavement under fatigue load and freeze-thaw coupling in cold climatic areas, *Construction and Building Materials*, Vol. 160, 588-597, doi:[10.1016/j.conbuildmat.2017.11.031](https://doi.org/10.1016/j.conbuildmat.2017.11.031)
- [11] Wu, S.-S.; Fang, Q.; Zhang, H.-G.; Gu, P.-Y.; Li, H. (2025). Investigation of damage mechanism of sawdust-magnesium oxychloride cement composites under uniaxial compressive load using AE and DIC techniques, *Construction and Building Materials*, Vol. 496, Paper 143762, 17 pages, doi:[10.1016/j.conbuildmat.2025.143762](https://doi.org/10.1016/j.conbuildmat.2025.143762)
- [12] Cao, F.; Qiao, H.-X.; Wang, P.-H.; Li, W.-J.; Li, Y.-K. (2022). Frost resistance of magnesium oxychloride cement mortar added with highland barley straw ash, *Journal of Wuhan University of Technology (Materials Science Edition)*, Vol. 37, No. 5, 912-921, doi:[10.1007/s11595-022-2614-z](https://doi.org/10.1007/s11595-022-2614-z)
- [13] Ahmad, F.; Rawat, S.; Yang, R. C.; Zhang, L.-H.; Guo, Y.-Y.; Fanna, D. J.; Zhang, Y. X. (2024). Effect of hybrid fibres on mechanical behaviour of magnesium oxychloride cement-based composites, *Construction and Building Materials*, Vol. 424, Paper 135937, 15 pages, doi:[10.1016/j.conbuildmat.2024.135937](https://doi.org/10.1016/j.conbuildmat.2024.135937)
- [14] Kia, A.; Wong, H. S.; Cheeseman, C. R. (2022). Freeze-thaw durability of conventional and novel permeable pavement replacement, *Journal of Transportation Engineering, Part B: Pavements*, Vol. 148, No. 4, Paper 04022051, doi:[10.1061/JPEODX.0000395](https://doi.org/10.1061/JPEODX.0000395)
- [15] Hanjari, K. Z.; Utgenannt, P.; Lundgren, K. (2011). Experimental study of the material and bond properties of frost-damaged concrete, *Cement and Concrete Research*, Vol. 41, No. 3, 244-254, doi:[10.1016/j.cemconres.2010.11.007](https://doi.org/10.1016/j.cemconres.2010.11.007)
- [16] Sun, L.-C.; Lou, P.-J.; Pan, C.; Ji, P.-H. (2024). A study on microscopic damage characteristics of freeze-thaw sandstone cyclic loading and unloading based on DEM, *Frontiers in Materials*, Vol. 11, Paper 1521874, 20 pages, doi:[10.3389/fmats.2024.1521874](https://doi.org/10.3389/fmats.2024.1521874)

- [17] Thomas, J.; Thaickavil, N. N.; Wilson, P. M. (2018). Strength and durability of concrete containing recycled concrete aggregates, *Journal of Building Engineering*, Vol. 19, 349-365, doi:[10.1016/j.jobe.2018.05.007](https://doi.org/10.1016/j.jobe.2018.05.007)
- [18] Nazeer, M.; Kapoor, K.; Singh, S. P. (2025). Strength, durability and microstructural properties of geopolymer pervious concrete containing recycled concrete aggregates, *Magazine of Concrete Research*, Vol. 77, Nos. 7-8, 371-383, doi:[10.1680/jmacr.24.00160](https://doi.org/10.1680/jmacr.24.00160)
- [19] Ayaz, M.; Suleiman, G. S. A.; Altaf, M.; Zafar, A. M.; Cheng, X.-S.; Feng, Y.-K. (2026). Polymer and eco-friendly inhibitors for corrosion protection of reinforced concrete: a comprehensive review, *Journal of Building Engineering*, Vol. 119, Paper 115119, 38 pages, doi:[10.1016/j.jobe.2025.115119](https://doi.org/10.1016/j.jobe.2025.115119)
- [20] Wang, S. R.; Zhao, J. Q.; Wu, X. G.; Yang, J. H.; Liu, A. (2021). Meso-scale simulations of lightweight aggregate concrete under impact loading, *International Journal of Simulation Modelling*, Vol. 20, No. 2, 291-302, doi:[10.2507/IJSIMM20-2-558](https://doi.org/10.2507/IJSIMM20-2-558)
- [21] Hasnat, A.; Ghafoori, N. (2021). Freeze-thaw resistance of nonproprietary ultrahigh-performance concrete, *Journal of Cold Regions Engineering*, Vol. 35, No. 3, Paper 04021008, doi:[10.1061/\(ASCE\)CR.1943-5495.0000255](https://doi.org/10.1061/(ASCE)CR.1943-5495.0000255)
- [22] Jafari, K.; Heidarneshad, F.; Moammer, O.; Jarrah, M. (2021). Experimental investigation on freeze-thaw durability of polymer concrete, *Frontiers of Structural and Civil Engineering*, Vol. 15, No. 4, 1038-1046, doi:[10.1007/s11709-021-0748-2](https://doi.org/10.1007/s11709-021-0748-2)
- [23] Wang, S.-R.; Cheng, C.-J.; Gong, J.; Song, Z.-H. (2025). Dynamic mechanical properties of magnesium oxychloride-based titanium gypsum concrete after high-temperature exposure, *Construction and Building Materials*, Vol. 472, Paper 140841, 15 pages, doi:[10.1016/j.conbuildmat.2025.140841](https://doi.org/10.1016/j.conbuildmat.2025.140841)
- [24] Gong, J.; He, M.-C.; Zhang, J.-X.; Liang, W.-M.; Wang, S.-R. (2025). Dynamic impact mechanical properties of red sandstone based on digital image correlation method, *International Journal of Mining, Reclamation and Environment*, Vol. 39, No. 4, 293-308, doi:[10.1080/17480930.2024.2385891](https://doi.org/10.1080/17480930.2024.2385891)
- [25] Heydari, M.; Farrokh, E.; Khoshrou, S. H. (2024). Parameter determination of Johnson-Holmquist-Cook constitutive model and calibration for Indiana Limestone, *Geomechanics and Geophysics for Geo-Energy and Geo-Resources*, Vol. 10, No. 1, Paper 122, 26 pages, doi:[10.1007/s40948-024-00845-y](https://doi.org/10.1007/s40948-024-00845-y)
- [26] Tai, Y.-S.; Tang, C.-C. (2006). Numerical simulation: the dynamic behavior of reinforced concrete plates under normal impact, *Theoretical and Applied Fracture Mechanics*, Vol. 45, No. 2, 117-127, doi:[10.1016/j.tafmec.2006.02.007](https://doi.org/10.1016/j.tafmec.2006.02.007)